

Band Structure of Overdoped Cuprate Superconductors: Density Functional Theory Matching Experiments

K. P. Kramer,¹ M. Horio,¹ S. S. Tsirkin,¹ Y. Sassa,² K. Hauser,¹ C. E. Matt,^{1,3} D. Sutter,¹ A. Chikina,³ N. Schröter,³ J. A. Krieger,^{4,5} T. Schmitt,³ V. N. Strocov,³ N. Plumb,³ M. Shi,³ S. Pyon,⁶ T. Takayama,⁶ H. Takagi,⁶ T. Adachi,⁷ T. Ohgi,⁸ T. Kawamata,⁸ Y. Koike,⁸ T. Kondo,⁹ O. J. Lipscombe,¹⁰ S. M. Hayden,¹⁰ M. Ishikado,¹¹ H. Eisaki,¹² T. Neupert,¹ and J. Chang¹

¹*Physik-Institut, Universität Zürich, Winterthurerstrasse 190, CH-8057 Zürich, Switzerland*

²*Department of Physics and Astronomy, Uppsala University, SE-75121 Uppsala, Sweden*

³*Swiss Light Source, Paul Scherrer Institut, CH-5232 Villigen PSI, Switzerland*

⁴*Laboratory for Muon Spin Spectroscopy, Paul Scherrer Institute, CH-5232 Villigen PSI, Switzerland*

⁵*Laboratorium für Festkörperphysik, ETH Zürich, CH-8093 Zürich, Switzerland*

⁶*Department of Advanced Materials, University of Tokyo, Kashiwa 277-8561, Japan*

⁷*Department of Engineering and Applied Sciences, Sophia University, Tokyo 102-8554, Japan*

⁸*Department of Applied Physics, Tohoku University, Sendai 980-8579, Japan*

⁹*ISSP, University of Tokyo, Kashiwa, Chiba 277-8581, Japan*

¹⁰*H. H. Wills Physics Laboratory, University of Bristol, Bristol BS8 1TL, United Kingdom*

¹¹*Comprehensive Research Organization for Science and Society (CROSS), Tokai, Ibaraki 319-1106, Japan*

¹²*Electronics and Photonics Research Institute, National Institute of Advanced Industrial Science and Technology, Ibaraki 305-8568, Japan*

A comprehensive angle resolved photoemission spectroscopy study of the band structure in single layer cuprates is presented with the aim of uncovering universal trends across different materials. Five different hole- and electron-doped cuprate superconductors ($\text{La}_{1.59}\text{Eu}_{0.2}\text{Sr}_{0.21}\text{CuO}_4$, $\text{La}_{1.77}\text{Sr}_{0.23}\text{CuO}_4$, $\text{Bi}_{1.74}\text{Pb}_{0.38}\text{Sr}_{1.88}\text{CuO}_{6+\delta}$, $\text{Tl}_2\text{Ba}_2\text{CuO}_{6+\delta}$, and $\text{Pr}_{1.15}\text{La}_{0.7}\text{Ce}_{0.15}\text{CuO}_4$) have been studied with special focus on the bands with predominately d -orbital character. Using light polarization analysis, the e_g and t_{2g} bands are identified across these materials. A clear correlation between the $d_{3z^2-r^2}$ band energy and the apical oxygen distance d_A is demonstrated. Moreover, the compound dependence of the $d_{x^2-y^2}$ band bottom and the t_{2g} band top is revealed. Direct comparison to density functional theory (DFT) calculations employing hybrid exchange-correlation functionals demonstrates excellent agreement. We thus conclude that the DFT methodology can be used to describe the global band structure of overdoped single layer cuprates on both the hole and electron doped side.

Introduction: The physics of cuprate superconductors has been a subject of intense investigations for more than three decades [1–3]. Yet, some of the most fundamental questions related to high-temperature superconductivity remain open. For example, consensus on the mechanism underpinning cuprate superconductivity is still missing. Related to this is the question of the defining parameters for the transition temperature T_c [4–9], and how to optimize it. Starting point for most theoretical approaches to superconductivity is an (effective) electronic band structure as well as the interactions that are relevant for driving a pairing mechanism. The former is typically obtained through density functional theory (DFT). However, because DFT cannot describe all relevant aspects of the electronic structure (such as the Mott insulating phase out of which superconductivity emerges upon hole or electron doping [10]) it is commonly viewed as too simplistic of an approach in the context of the cuprates [11]. Another widespread assumption is that effective models for cuprates can be constructed solely on the $d_{x^2-y^2}$ band structure. This latter assumption has recently been challenged [6, 12] by angle-resolved photoemission spectroscopy (ARPES) observations of a second band ($d_{3z^2-r^2}$) hybridizing with the $d_{x^2-y^2}$ orbital

in overdoped $\text{La}_{1.77}\text{Sr}_{0.23}\text{CuO}_4$ (LSCO) [7, 13].

Here we provide a systematic ARPES and DFT study of the electronic d -band structure across single layer cuprate superconductors. Five different hole- and electron-overdoped superconducting systems [$\text{La}_{1.59}\text{Eu}_{0.2}\text{Sr}_{0.21}\text{CuO}_4$ (Eu-LSCO), $\text{La}_{1.77}\text{Sr}_{0.23}\text{CuO}_4$ (LSCO), $\text{Bi}_{1.74}\text{Pb}_{0.38}\text{Sr}_{1.88}\text{CuO}_{6+\delta}$ (Bi2201), $\text{Tl}_2\text{Ba}_2\text{CuO}_{6+\delta}$ (Tl2201), and $\text{Pr}_{1.15}\text{La}_{0.7}\text{Ce}_{0.15}\text{CuO}_4$ (PLCCO)] have been investigated experimentally. This has led to three main observations: (i) clear identification of the $d_{3z^2-r^2}$ band position in three of the mentioned compounds, (ii) compound dependence of the $d_{x^2-y^2}$ band bottom positions and (iii) the t_{2g} (d_{xy} , d_{xz} and d_{yz}) band positions at the zone corner. These experimental observations are quantified as a function of apical oxygen distance d_A and compared directly to DFT calculations. Generally, excellent quantitative agreement between DFT and experimental band structures is found. It is therefore concluded that even though DFT is not capturing low-energy self-energy effects, it is successfully describing the global band structure of the cuprates.

Methods: Single crystals of Eu-LSCO, LSCO, Bi2201, Tl2201 and PLCCO were grown by floating zone or flux

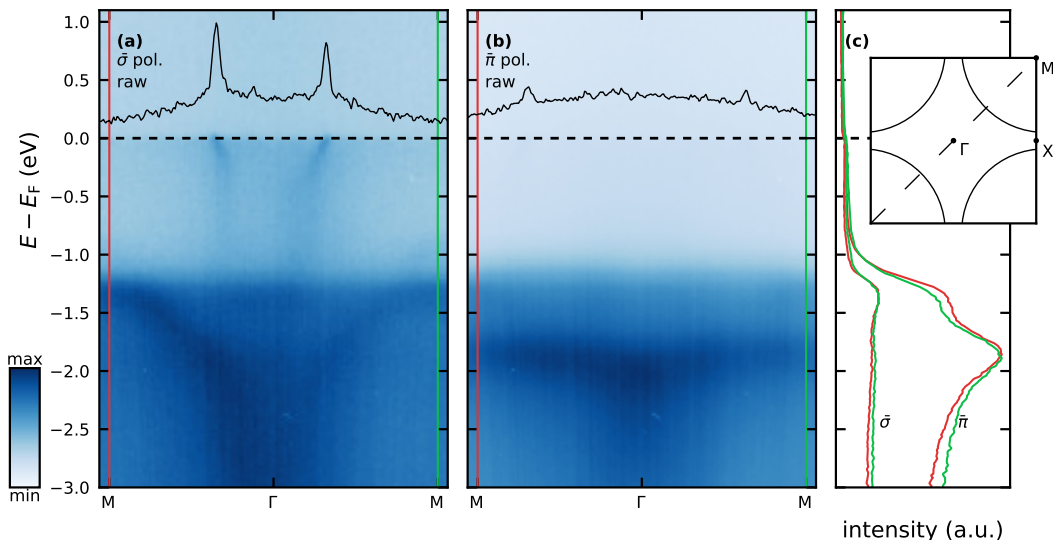


FIG. 1. Nodal soft x-ray ARPES spectra recorded on $\text{Bi}_{1.74}\text{Pb}_{0.38}\text{Sr}_{1.88}\text{CuO}_{6+\delta}$ with 420 eV incident photons of different linear polarizations, as indicated. (a),(b) Recorded ARPES spectra along the line $\overline{\text{M}\Gamma\text{M}}$ (dashed line in the inset of (c)) for $\bar{\sigma}$ - and $\bar{\pi}$ -polarized light, respectively. Depicted at the top are momentum distribution curves taken at the Fermi level E_{F} . (c) Energy distribution curves taken along vertical lines of corresponding colors in (a) and (b). Inset: schematic of the Fermi surface with the diagonal (nodal) direction indicated as a dashed line.

growth techniques. Both ultraviolet (20–200 eV) and soft x-ray (200–600 eV) ARPES experiments were carried out at the SIS [14] and ADDRESS [15] beamlines at the Swiss Light Source. All data were recorded at a temperature of approximately 20 K. Electrons were analyzed through a slit oriented within the photoemission mirror plane [16]. Light polarization perpendicular (parallel) to the mirror plane is denoted as $\bar{\sigma}$ ($\bar{\pi}$).

Predicting the correct energies for the electronic bands is a notorious problem for DFT in many materials, which is mostly due to the unknown form of the exchange-correlation functional. Improvements over local density approximations are commonly obtained using hybrid functionals which mix in a portion α of exact exchange from Hartree-Fock theory [17]. While α is a free parameter in general, we find good agreement between the theoretical and experimental band structures for all compounds studied by fixing $\alpha = 0.1$. We thus propose this value as generically suited for cuprate superconductors. A hypothetical tetragonal structure of La_2CuO_4 with lattice parameters corresponding to overdoped LSCO was used and the chemical potential adjusted to match the actual hole-filling. Similarly, for Bi2201, Tl2201 and PLCCO stoichiometric tetragonal crystal structures were used as a starting point for the DFT calculations. We ensured, on the example of Bi2201, that using an or-

thorhombic crystal structure leads to essentially the same results after downfolding the calculated band structure to the tetragonal Brillouin zone. More details on the methodology used can be found in the supplementary material [?]. Although some of the systems studied have orthorhombic structures, we represent all data in tetragonal notation [16], using the CuO_2 plaquette Brillouin zone nomenclature. Therefore M and X, respectively, denote the zone corner (1, 1) and boundary (1, 0) in units of π/a with a being the tetragonal in-plane lattice parameter [Fig. 1 (c), inset].

Results: We start by examining the nodal spectra recorded on overdoped Bi2201 using linearly polarized soft x-rays, see Fig. 1. The photoemission intensities of the observed band structure are highly dependent on the incident light polarization. Three distinct bands are identified. (i) The intensely-studied nodal quasiparticle dispersion [18–20] crossing the Fermi level E_{F} , which is observed with $\bar{\sigma}$ -polarized light only. This fact can be appreciated both from the energy distribution maps (EDMs) and the momentum distribution curves (MDCs) at the Fermi level [Figs. 1 (a),(b)]. (ii) A second dispersive band with energy maximum of -1.3 eV at the M-point and band bottom at the Γ -point. At the M-point, this band is featured in both the $\bar{\sigma}$ and $\bar{\pi}$ channels [Fig. 1 (c)]. Notice that in comparison to previous stud-

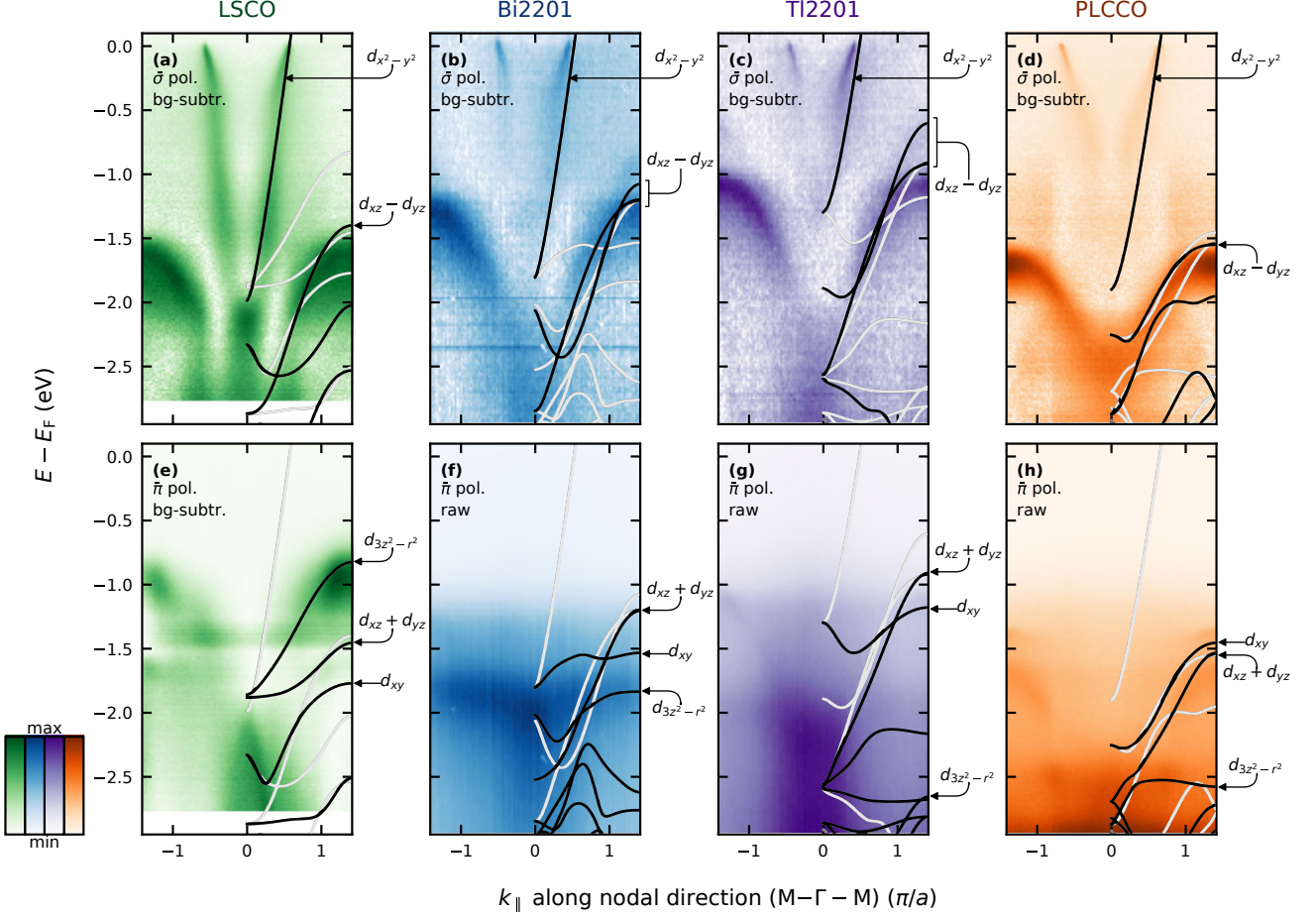


FIG. 2. Nodal ARPES spectra and DFT band structure calculations for the single-layer cuprates $\text{La}_{1.77}\text{Sr}_{0.23}\text{CuO}_4$, $\text{Bi}_{1.74}\text{Pb}_{0.38}\text{Sr}_{1.88}\text{CuO}_{6+\delta}$, $\text{Tl}_2\text{Ba}_2\text{CuO}_{6+\delta}$ and $\text{Pr}_{1.15}\text{La}_{0.7}\text{Ce}_{0.15}\text{CuO}_4$. (a)–(d) Background subtracted nodal ARPES spectra recorded using $\bar{\sigma}$ -polarized light. (e)–(h) Nodal spectra recorded with $\bar{\pi}$ -polarized light. The spectrum in (e) has received the same background subtraction as the ones in (a) – (d). By contrast, the spectra in panels (f) – (h) represent raw data as the background subtraction methodology is not advised in presence of flat bands (see text and discussion in suppl. Fig. S3). The calculated DFT band structure is overlaid with solid lines where black and light grey colors indicate finite or zero matrix elements, respectively. The labeling of the orbital character is only valid at the M point for the cases of d_{xz} , d_{xy} and d_{yz} . See suppl. Fig. S2 for a full orbital character assignment.

ies of Bi2201, our data displays extremely weak (π, π) -folded replica bands [21, 22]. As a result and in contrast to Refs. 23 and 24, this dispersive band is not found at the (π, π) -folded equivalent Γ -point. (iii) The $\bar{\pi}$ -channel features an additional weakly dispersive band at energy -1.8 eV [Fig. 1 (b)]. This band, which to the best of our knowledge has not been reported previously, is completely suppressed in the $\bar{\sigma}$ -sector.

Nodal ARPES spectra recorded in $\bar{\sigma}$ and $\bar{\pi}$ polarization on LSCO, Bi2201, Tl2201 and PLCCO are shown in Figs. 2 (a)–(h). For all four compounds, the band crossing the Fermi level is visible (suppressed) in the $\bar{\sigma}$ ($\bar{\pi}$) channel. Interestingly, the bottom of this band

varies significantly, from -2 eV in LSCO to -1.25 eV for Tl2201. In the $\bar{\pi}$ channel an additional band feature appears for LSCO, Bi2201 and PLCCO. The position and band width of this $\bar{\sigma}$ -suppressed band differs for the three compounds. In LSCO, it disperses from -0.9 eV at the M-point to -1.5 eV at the zone center, while for Bi2201 and PLCCO the $\bar{\pi}$ -branches found at -1.8 eV and -2.5 eV respectively, are quasi non-dispersive. Finally, for Tl2201 no band unique to the $\bar{\pi}$ channel was identified down to -3 eV.

The DFT band structure of LSCO, Bi2201, Tl2201 and PLCCO [Figs. 2 (a)–(h)] has been calculated as described above and in the supplementary material. In ad-

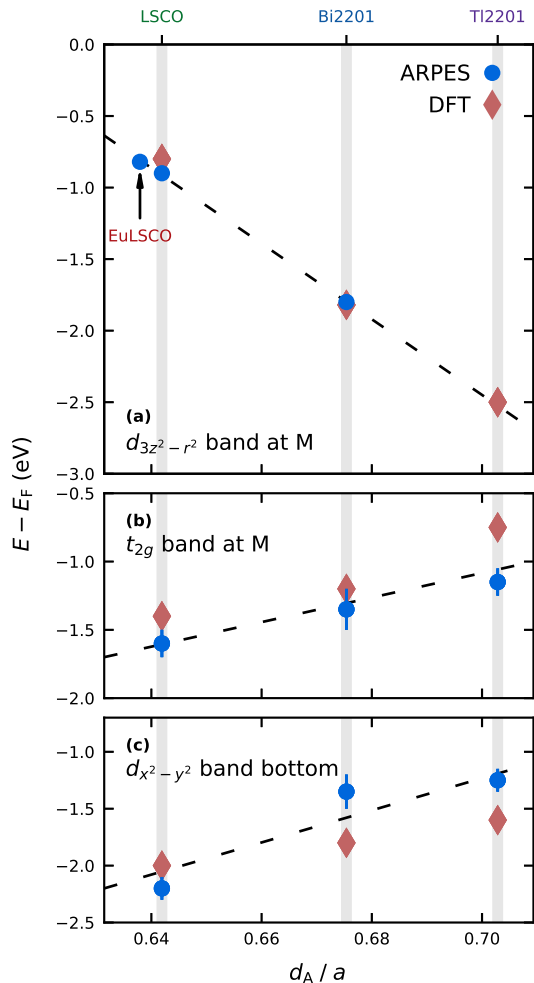


FIG. 3. Band structure characteristics versus ratio between apical oxygen distance and (tetragonal) in-plane lattice constant d_A/a . Blue points represent the ARPES experiments whereas results from our DFT calculations are indicated by red diamonds. Dashed lines represent guides to the eye. (a) $d_{3z^2-r^2}$ band position at the M point versus d_A/a . (b) Position of the t_{2g} band at the zone corner M versus d_A/a . Mean values of the d_{xy} , $d_{xz}+d_{yz}$ and $d_{xz}-d_{yz}$ band positions at M are taken for the DFT points. (c) $d_{x^2-y^2}$ band bottom as function of d_A/a .

dition to the band dispersions, their expected photoemission matrix elements are indicated according to their mirror eigenvalues. To first order, photoemission matrix elements can be understood through simple symmetry considerations [16, 25]. Our experimental setup has a mirror-plane defined by the incident photon beam and the electron analyzer. With respect to this plane, the electromagnetic field \mathbf{A} has even (odd) parity for parallel (perpendicular) $\bar{\pi}$ ($\bar{\sigma}$) polarization [suppl. Figs. S4 (a), (b)]. Meanwhile, the photoemitted electron wave func-

tion has even parity. The mirror eigenvalues of the ($d_{x^2-y^2}$, $d_{3z^2-r^2}$, d_{xy} , $d_{xz}+d_{yz}$, $d_{xz}-d_{yz}$) orbital states are $(-1, 1, 1, 1, -1)$, respectively (suppl. Tab. SI). Therefore, $d_{3z^2-r^2}$ and d_{xy} states will be suppressed in the $\bar{\sigma}$ channel while $d_{x^2-y^2}$ states cannot appear under $\bar{\pi}$ illumination. Since d_{xz} and d_{yz} orbitals are not eigenstates of the mirror operator, electronic states along $\bar{\Gamma M}$ are formed by even ($d_{xz} + d_{yz}$) and odd ($d_{xz} - d_{yz}$) linear combinations and will thus be visible under both polarizations. In Fig. 2, bands with matrix element 0 are colored light grey, while bands with nonzero matrix element remain black.

For LSCO, the $d_{3z^2-r^2}$ band width is roughly 0.5 eV with a band maximum at the M-point (-0.8 eV). The crossing of the $d_{3z^2-r^2}$ and $d_{x^2-y^2}$ bands, constituting a type-II Dirac line node, is protected by mirror symmetry [13, 26]. For Bi2201 and Tl2201, the $d_{3z^2-r^2}$ band is pushed to lower energies and an overall smaller $d_{3z^2-r^2}$ band width is found. As a result, the nodal crossing of the $d_{3z^2-r^2}$ and $d_{x^2-y^2}$ bands is not found for Bi2201 and Tl2201. The type-II Dirac line node is thus unique to LSCO [13]. We also notice that in LSCO, the $d_{3z^2-r^2}$ band lies above the t_{2g} bands whereas the opposite is true for Bi2201 and Tl2201. Finally, in comparison to LSCO, the bottom of the $d_{x^2-y^2}$ band is closer to the Fermi level in Tl2201.

Discussion: The polarization dependence of the band which crosses the Fermi level allows us to assign it uniquely to the $d_{x^2-y^2}$ orbital in all studied compounds. For Bi2201, the next band below the Fermi level is found in both the $\bar{\sigma}$ and $\bar{\pi}$ channels and hence can be assigned to the d_{xz} , d_{yz} orbitals. The flat band found around -1.8 eV in the $\bar{\pi}$ channel has to have either d_{xy} or $d_{3z^2-r^2}$ character. For a unique orbital assignment we stress the following facts: (i) Resonant inelastic x-ray scattering (RIXS) measurements of the dd -excitations found the $d_{3z^2-r^2}$ states at -2 eV and below the d_{xy} , d_{xz} , d_{yz} states [27]. (ii) As the d_{xy} orbital extends purely in the xy -plane, the d_{xy} band is generally expected to disperse strongly along the nodal direction. This is indeed confirmed by our DFT calculations. Combined, this lets us assign the -1.8 eV band in Bi2201 to the $d_{3z^2-r^2}$ orbital. As previously discussed in Ref. 7 and shown in Fig. 2 and suppl. Fig. S3 the $d_{3z^2-r^2}$ band is clearly identified in La-based cuprates. In the case of Tl2201, by contrast, no evidence for the $d_{3z^2-r^2}$ band is found down to -3 eV. Therefore, either the $d_{3z^2-r^2}$ band in Tl2201 is pushed to even lower binding energies or this band is too faint to be observed. The latter scenario is supported by the fact that in PLCCO with no apical oxygen, the $d_{3z^2-r^2}$ band is found at around -2.5 eV [see Fig. 2(h)].

We plot the observed $d_{3z^2-r^2}$ band position at the M-point as a function of the compound dependent ratio between apical oxygen distance d_A and in-plane lattice constant a (Fig. 3). Furthermore, the $d_{x^2-y^2}$ band bottoms and the energies of the t_{2g} bands at the zone corner

M are plotted alongside their respective positions found from our DFT calculations. One can see that the calculations capture the most salient band structure trends: (i) DFT correctly predicts how the $d_{3z^2-r^2}$ band position – with respect to the Fermi level – evolves as a function of d_A/a . (ii) DFT yields the right trends for the band widths of both the $d_{3z^2-r^2}$ and $d_{x^2-y^2}$ bands. The $d_{3z^2-r^2}$ band width is, for example, gradually reduced when going through the series LSCO \rightarrow Bi2201 \rightarrow Tl2201. The ARPES data on LSCO and Bi2201 supports that trend. For the $d_{x^2-y^2}$ band, ARPES only reveals the occupied part. Instead of band width, it thus makes more sense to consider the band bottom. It turns out that the $d_{x^2-y^2}$ band minimum is varying across LSCO, Bi2201, and Tl2201 and the positions agree between DFT and experiment. (iii) The t_{2g} band position at the zone corner also follows the trend of moving closer to E_F with increasing d_A/a , both in experiment and the DFT calculations. However, we stress that because the DFT methodology is not including electron interactions, it is not capturing self-energy effects such as the much discussed nodal waterfall structure [28–30].

Conclusions: In summary, we have carried out a comprehensive ARPES and DFT study of the band structure across single layer cuprate superconductors. Experimentally, five different overdoped cuprate compounds were studied using light polarization analysis to assign band orbital characters. Both the e_g ($d_{x^2-y^2}$ and $d_{3z^2-r^2}$) and t_{2g} bands were discussed and their band positions and band widths were compared to DFT calculations. The excellent agreement between DFT and experimental results led us to conclude that the DFT methodology with proper choice of exchange-correlation functional does capture the global electronic structure of the overdoped cuprates.

Acknowledgments: K.P.K., M.H., D.S., J.A.K., and J.C. acknowledge support by the Swiss National Science Foundation. Y.S. is funded by the Swedish Research Council (VR) with a Starting Grant (Dnr. 2017-05078) O.K.F. and M.M. are supported by a VR neutron project grant (BIFROST, Dnr. 2016-06955). ARPES measurements were performed at the ADDRESS and SIS beamlines of the Swiss Light Source at the Paul Scherrer Institute. We thank the beamline staff for their support.

-
- [1] P. A. Lee, N. Nagaosa, and X.-G. Wen, *Rev. Mod. Phys.* **78**, 17 (2006), URL <https://link.aps.org/doi/10.1103/RevModPhys.78.17>.
- [2] B. Keimer, S. A. Kivelson, M. R. Norman, S. Uchida, and J. Zaanen, *Nature* **518**, 179 EP (2015), URL <http://dx.doi.org/10.1038/nature14165>.
- [3] D. J. Scalapino, *Rev. Mod. Phys.* **84**, 1383 (2012), URL <https://link.aps.org/doi/10.1103/RevModPhys.84.1383>.
- [4] J. A. Slezak, J. Lee, M. Wang, K. McElroy, K. Fujita, B. M. Andersen, P. J. Hirschfeld, H. Eisaki, S. Uchida, and J. C. Davis, *Proceedings of the National Academy of Sciences of the United States of America* **105**, 3203 (2008), ISSN 0027-8424.
- [5] M. R. Norman, *Proceedings of the National Academy of Sciences* **105**, 3173 (2008), ISSN 0027-8424, <http://www.pnas.org/content/105/9/3173.full.pdf>, URL <http://www.pnas.org/content/105/9/3173>.
- [6] H. Sakakibara, H. Usui, K. Kuroki, R. Arita, and H. Aoki, *Phys. Rev. Lett.* **105**, 057003 (2010), URL <http://link.aps.org/doi/10.1103/PhysRevLett.105.057003>.
- [7] C. E. Matt, D. Sutter, A. M. Cook, Y. Sassa, M. Månsson, O. Tjernberg, L. Das, M. Horio, D. Destraz, C. G. Fatuzzo, et al., *Nat. Commun.* **9**, 972 (2018).
- [8] C. Weber, C. Yee, K. Haule, and G. Kotliar, *EPL (Europhysics Letters)* **100**, 37001 (2012), URL <http://stacks.iop.org/0295-5075/100/i=3/a=37001>.
- [9] R. Adler, C.-J. Kang, C.-H. Yee, and G. Kotliar, *ArXiv e-prints* (2018), 1807.00398.
- [10] J. W. Furness, Y. Zhang, C. Lane, I. G. Buda, B. Barbiellini, R. S. Markiewicz, A. Bansil, and J. Sun, *Communications Physics* **1**, 11 (2018), URL <https://doi.org/10.1038/s42005-018-0009-4>.
- [11] L. Hozoi, L. Siurakshina, P. Fulde, and J. van den Brink, *Scientific Reports* **1**, 65 (2011), URL <http://dx.doi.org/10.1038/srep00065>.
- [12] H. Sakakibara, H. Usui, K. Kuroki, R. Arita, and H. Aoki, *Phys. Rev. B* **85**, 064501 (2012), URL <http://link.aps.org/doi/10.1103/PhysRevB.85.064501>.
- [13] M. Horio, C. E. Matt, K. Kramer, D. Sutter, A. M. Cook, Y. Sassa, K. Hauser, M. Månsson, N. C. Plumb, M. Shi, et al., *Nature Communications* **9**, 3252 (2018), URL <https://doi.org/10.1038/s41467-018-05715-2>.
- [14] L. P. U. Flechsig and T. Schmidt, *AIP Conf. Proc.* **705**, 316 (2004).
- [15] V. N. Strocov, X. Wang, M. Shi, M. Kobayashi, J. Krenpasky, C. Hess, T. Schmitt, and L. Patthey, *J. Synchrotron Rad.* **21**, 32 (2014), URL <https://doi.org/10.1107/S1600577513019085>.
- [16] A. Damascelli, Z. Hussain, and Z.-X. Shen, *Rev. Mod. Phys.* **75**, 473 (2003).
- [17] A. V. Krukau, O. A. Vydrov, A. F. Izmaylov, and G. E. Scuseria, *The Journal of Chemical Physics* **125**, 224106 (2006), <https://doi.org/10.1063/1.2404663>, URL <https://doi.org/10.1063/1.2404663>.
- [18] X. J. Zhou, T. Yoshida, A. Lanzara, P. V. Bogdanov, S. A. Kellar, K. M. Shen, W. L. Yang, F. Ronning, T. Sasagawa, T. Kakeshita, et al., *Nature* **423**, 398 (2003), URL <http://dx.doi.org/10.1038/423398a>.
- [19] C. G. Fatuzzo, Y. Sassa, M. Månsson, S. Pailhès, O. J. Lipscombe, S. M. Hayden, L. Patthey, M. Shi, M. Grioni, H. M. Rønnow, et al., *Phys. Rev. B* **89**, 205104 (2014), URL <https://link.aps.org/doi/10.1103/PhysRevB.89.205104>.
- [20] T. Yoshida, X. J. Zhou, D. H. Lu, S. Komiyama, Y. Ando, H. Eisaki, T. Kakeshita, S. Uchida, Z. Hussain, Z.-X. Shen, et al., *J. Phys. Condens. Matter* **19**, 125209 (2007).
- [21] P. D. C. King, J. A. Rosen, W. Meevasana, A. Tamai, E. Rozbicki, R. Comin, G. Levy, D. Fournier, Y. Yoshida, H. Eisaki, et al., **106**, 127005 (2011), URL <https://link.aps.org/doi/10.1103/PhysRevLett.106.127005>.

- [22] J. A. Rosen, R. Comin, G. Levy, D. Fournier, Z. H. Zhu, B. Ludbrook, C. N. Veenstra, A. Nicolaou, D. Wong, P. Dosanjh, et al., *Nature Communications* **4**, 1977 EP (2013), URL <http://dx.doi.org/10.1038/ncomms2977>.
- [23] J. Xia, E. Schemm, G. Deutscher, S. A. Kivelson, D. A. Bonn, W. N. Hardy, R. Liang, W. Siemons, G. Koster, M. M. Fejer, et al., *Phys. Rev. Lett.* **100**, 127002 (2008), URL <https://link.aps.org/doi/10.1103/PhysRevLett.100.127002>.
- [24] W. Meevasana, X. J. Zhou, S. Sahrakorpi, W. S. Lee, W. L. Yang, K. Tanaka, N. Mannella, T. Yoshida, D. H. Lu, Y. L. Chen, et al., *Phys. Rev. B* **75**, 174506 (2007), URL <https://link.aps.org/doi/10.1103/PhysRevB.75.174506>.
- [25] S. Moser, *Journal of Electron Spectroscopy and Related Phenomena* **214**, 29 (2017), ISSN 0368-2048, URL <http://www.sciencedirect.com/science/article/pii/S0368204816301724>.
- [26] L. L. Tao and E. Y. Tsymbal, *Phys. Rev. B* **98**, 121102 (2018), URL <https://link.aps.org/doi/10.1103/PhysRevB.98.121102>.
- [27] Y. Y. Peng, G. Dellea, M. Minola, M. Conni, A. Amorese, D. Di Castro, G. M. De Luca, K. Kummer, M. Salluzzo, X. Sun, et al., *Nature Physics* **13**, 1201 EP (2017), URL <http://dx.doi.org/10.1038/nphys4248>.
- [28] J. Graf, G.-H. Gweon, K. McElroy, S. Y. Zhou, C. Jozwiak, E. Rotenberg, A. Bill, T. Sasagawa, H. Eisaki, S. Uchida, et al., *Phys. Rev. Lett.* **98**, 067004 (2007), URL <https://link.aps.org/doi/10.1103/PhysRevLett.98.067004>.
- [29] T. Valla, T. E. Kidd, W.-G. Yin, G. D. Gu, P. D. Johnson, Z.-H. Pan, and A. V. Fedorov, *Phys. Rev. Lett.* **98**, 167003 (2007), URL <https://link.aps.org/doi/10.1103/PhysRevLett.98.167003>.
- [30] J. Chang, S. Pailh s, M. Shi, M. M nsson, T. Claesson, O. Tjernberg, J. Voigt, V. Perez, L. Patthey, N. Momono, et al., *Phys. Rev. B* **75**, 224508 (2007), URL <https://link.aps.org/doi/10.1103/PhysRevB.75.224508>.
- [31] G. Kresse and J. Hafner, *Phys. Rev. B* **48**, 13115 (1993), URL <https://link.aps.org/doi/10.1103/PhysRevB.48.13115>.
- [32] G. Kresse and J. Furthm ller, *Computational Materials Science* **6**, 15 (1996), ISSN 0927-0256, URL <http://www.sciencedirect.com/science/article/pii/0927025696000080>.
- [33] P. E. Bl chl, *Phys. Rev. B* **50**, 17953 (1994), URL <https://link.aps.org/doi/10.1103/PhysRevB.50.17953>.
- [34] G. Kresse and D. Joubert, *Phys. Rev. B* **59**, 1758 (1999), URL <https://link.aps.org/doi/10.1103/PhysRevB.59.1758>.
- [35] J. P. Perdew, K. Burke, and M. Ernzerhof, *Phys. Rev. Lett.* **77**, 3865 (1996), URL <https://link.aps.org/doi/10.1103/PhysRevLett.77.3865>.
- [36] A. A. Mostofi, J. R. Yates, Y.-S. Lee, I. Souza, D. Vanderbilt, and N. Marzari, *Computer Physics Communications* **178**, 685 (2008), ISSN 0010-4655, URL <http://www.sciencedirect.com/science/article/pii/S0010465507004936>.
- [37] A. A. Mostofi, J. R. Yates, G. Pizzi, Y.-S. Lee, I. Souza, D. Vanderbilt, and N. Marzari, *Comput. Phys. Commun.* **185**, 2309 (2014), ISSN 0010-4655.
- [38] A. Kaminski, S. Rosenkranz, H. M. Fretwell, J. Mesot, M. Randeria, J. C. Campuzano, M. R. Norman, Z. Z. Li, H. Raffy, T. Sato, et al., *Phys. Rev. B* **69**, 212509 (2004), URL <https://link.aps.org/doi/10.1103/PhysRevB.69.212509>.
- [39] M. Horio, K. Hauser, Y. Sassa, Z. Mingazheva, D. Sutter, K. Kramer, A. Cook, E. Nocerino, O. K. Forslund, O. Tjernberg, et al., *Physical Review Letters* **121**, 077004 (2018).

SUPPLEMENTARY INFORMATION

DFT calculations: The presented DFT calculations were performed using the VASP code package [31, 32] employing the projector-augmented wave method (PAW) [33, 34]. The exchange-correlation functional was treated in the form similar to the Heyd-Scuseria-Ernzerhof (HSE06) [17] screened hybrid functional, but with a variable portion α of Hartree-Fock (HF) exchange. The standard HSE06 functional uses $\alpha = 0.25$, i.e. 25% of HF exchange and 75% of Perdew, Burke, and Ernzerhof generalized-gradient approximation (GGA) [35] for the short-range part of the exchange functional. We discover that this tends to overestimate the binding energy of the bands in the materials under study. On the other hand the pure GGA functional ($\alpha = 0$) underestimates the binding energies. By varying the portion of HF exchange, we find that the best overall agreement for all investigated materials is achieved by letting $\alpha = 0.1$ (suppl. Fig. S1). After performing self-consistent hybrid-functional calculations on a regular 6x6x6 Γ -centered k-point grid, we interpolate the band structures along the $\bar{\Gamma}\bar{M}$ line by means of the Wannier90 code package [36, 37].

We add two notes concerning the calculations of PLCCO: (i) We started with the stoichiometric crystal structure of Pr_2CuO_4 and simulated the La occupation by replacing one of the two Pr sites in the unit cell with La. Even though this does not exactly represent the exact occupation that is present in the experimental compound, we ensured by comparison to calculations on Pr_2CuO_4 that varying the La content has only a minor effect on the electronic band structure. Thus the small error in occupation should not affect our conclusion. (ii) The energies of the 4*f*-bands resulting from our calculations lie above E_F due to the shifting of the Fermi level in order to account for the right electron filling. This result is of course unphysical and we conclude that our methodology, while proving very successful for the *d*-orbitals, is unfit to correctly predict the *f*-orbitals.

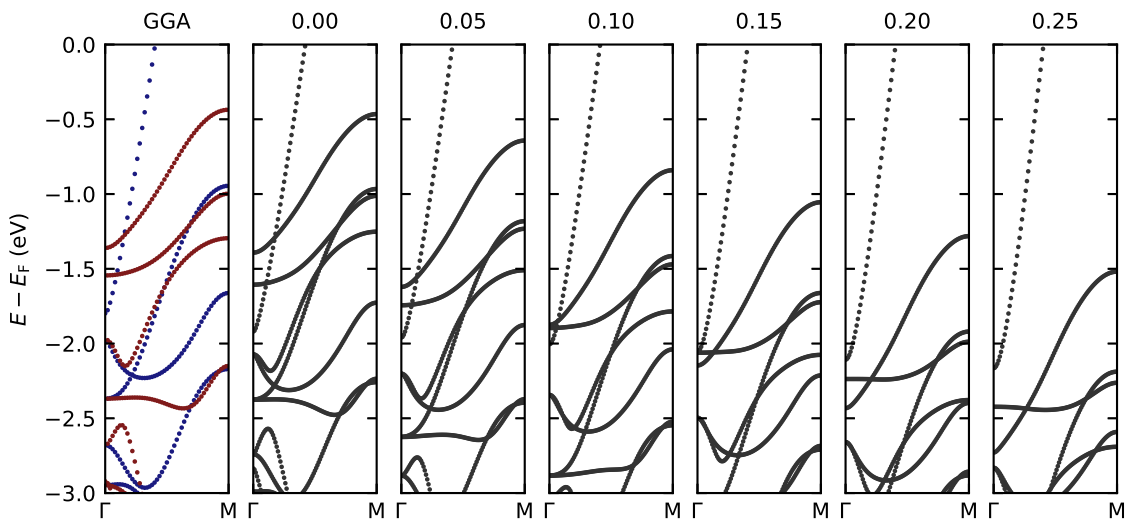


FIG. S1. DFT results for different values of the amount of exact exchange α as well as pure GGA at the example of LSCO. Red and blue colors denote mirror eigenvalues of +1 or -1 respectively.

Background subtraction: In virtually all spectroscopy methods, the obtained data contains an intrinsic and extrinsic background. For the cuprates, it has been demonstrated that these background contributions have significant dependencies on binding energy [38]. In fact, the background at binding energies of 1 eV might be an order of magnitude larger than at or near the Fermi level. For comparison of band structures across a wide range of binding energy, it can therefore be useful to subtract the background intensity [7]. Assuming a *k*-independent background, we estimate the background profile by averaging the five lowest intensity points of each MDC [7, 13]. In this fashion, we are subtracting a constant background at each binding energy. MDCs therefore remain unchanged. Two examples, using Eu-LSCO and Tl2201, of this background subtraction procedure are shown in supplementary Fig. S3. We stress that for flat non-dispersive bands such a background determination is not advisable as the band structure will be eliminated in the subtraction procedure. We therefore only apply the background subtraction, in Fig. 2 of the main text, to enhance the visibility of dispersive bands.

Experimental details: Eu-LSCO, LSCO and PLCCO data presented has been acquired at the SIS beamline with

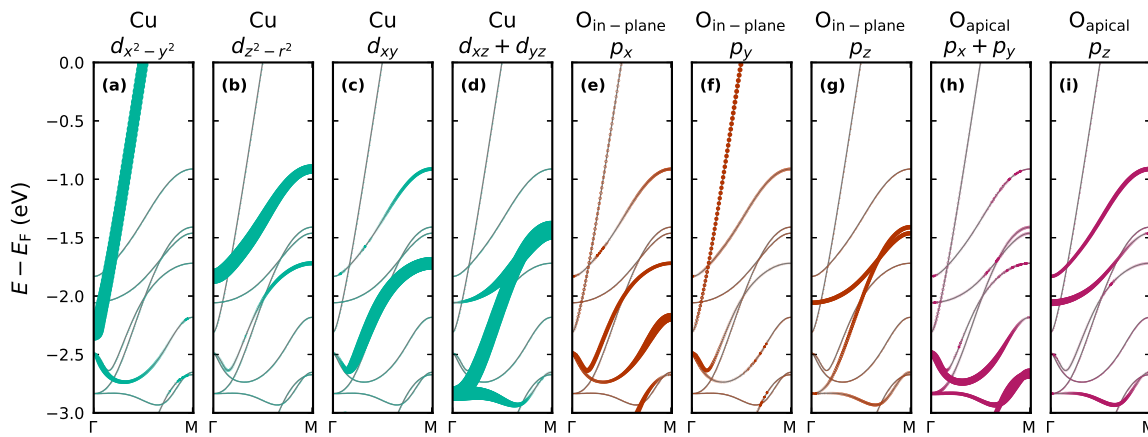


FIG. S2. Orbital weights given by DFT at the example of LSCO for the Cu d -orbitals [panels (a)–(d)], the in-plane Oxygen p -orbitals [(e)–(g)] and the apical (out-of-plane) oxygen p -orbitals [(h), (i)]. The marker area is proportional to the respective orbital weight. Other orbitals do not contribute significantly to the band structure in the shown energy range.

incident photon energies of 160 eV, 160 eV and 55 eV, respectively. Meanwhile, Bi2201 and Tl2201 data was taken at the ADDRESS beamline with photon energies of 420 eV and 428 eV, respectively. All data presented was acquired at a temperature of approximately 20 K. The used photon energies ensure that the data taken stems from planes through Γ along the k_z -direction for LSCO, Tl2201 and PLCCO. For Bi2201 we are closer to the Brillouin zone edge along the k_z -direction. Meanwhile, all calculations were done for $k_z = 0$, i.e. in planes through the Brillouin zone center. This fact does not invalidate our comparison between ARPES and DFT, however: The k_z -dispersion has been shown to be of very small (yet finite) order in LSCO [7, 39] and is not expected to be any bigger for Bi2201. The effect of being at a different k_z therefore only contributes a shift in the order of the marker size in Fig. 3 of the main text.

	$ d_j\rangle$	$ x^2 - y^2\rangle$	$ 3z^2 - r^2\rangle$	$ xy\rangle$	$ xz\rangle + yz\rangle$	$ xz\rangle - yz\rangle$
$\langle d_j M_{xy} d_j \rangle$		-1	+1	+1	+1	-1
Character		odd	even	even	even	odd
$\langle f A \epsilon_{\bar{\sigma}} d_j \rangle$		$\neq 0$	0	0	0	$\neq 0$
$\langle f A \epsilon_{\bar{\pi}} d_j \rangle$		0	$\neq 0$	$\neq 0$	$\neq 0$	0

TABLE SI. Connection between the orbital mirror symmetries and photoemission matrix elements. The first row gives the eigenvalues with respect to a mirror at the nodal plane M_{xy} for the d -orbitals in a basis in which M_{xy} is diagonal. The last two rows contain the photoemission matrix element as a function of d -orbital and incident light polarization. A denotes the magnitude of the electromagnetic vector potential. The polarization vector $\epsilon_{\bar{\sigma}}$ ($\epsilon_{\bar{\pi}}$) is perpendicular (parallel) to the analyzer plane and thus corresponds to $\bar{\sigma}$ -polarized ($\bar{\pi}$ -polarized) light of *odd* (*even*) character. The final state $\langle f |$ is assumed to be a plane wave of *even* character.

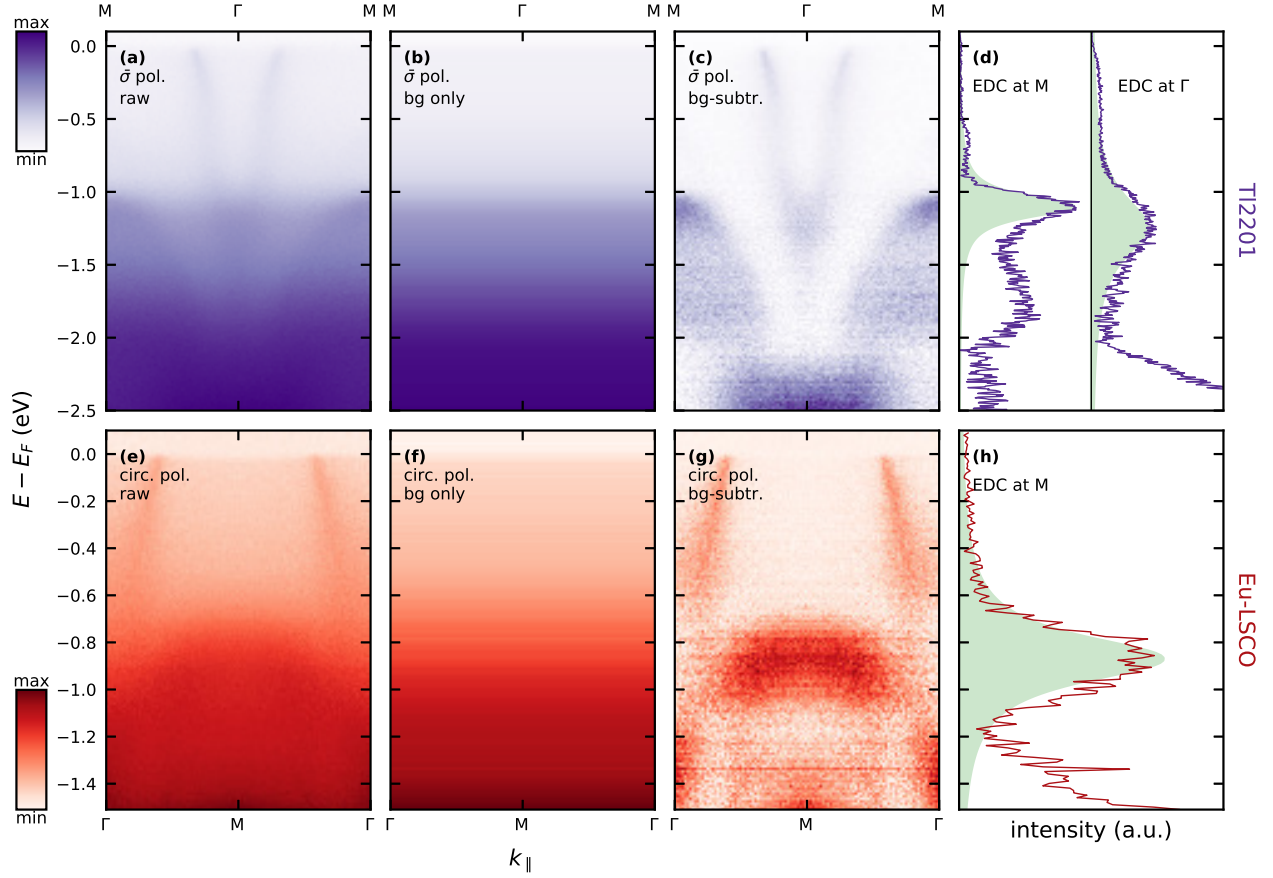


FIG. S3. Demonstration of background subtraction, exemplified by nodal spectra recorded on $\text{Tl}_2\text{Ba}_2\text{CuO}_{6+\delta}$ and $\text{La}_{1.59}\text{Eu}_{0.2}\text{Sr}_{0.21}\text{CuO}_4$. **(a),(e)** Raw nodal spectra for Tl2201 and Eu-LSCO respectively. **(b),(f)** Corresponding background profile extracted by averaging the lowest five points in every momentum distribution curve (see text). **(c),(g)** Resulting background subtracted energy distribution maps. **(d),(h)** Background subtracted energy distribution curves at the Γ - and/or M-point. In the case of Eu-LSCO, the data has been taken in the second Brillouin zone and was symmetrized around M. A power-law mapping $y = x^\gamma$ with $\gamma = 0.5$ has been applied to the colorscale in panels (a), (b), (e) and (f) in order to enhance visibility.

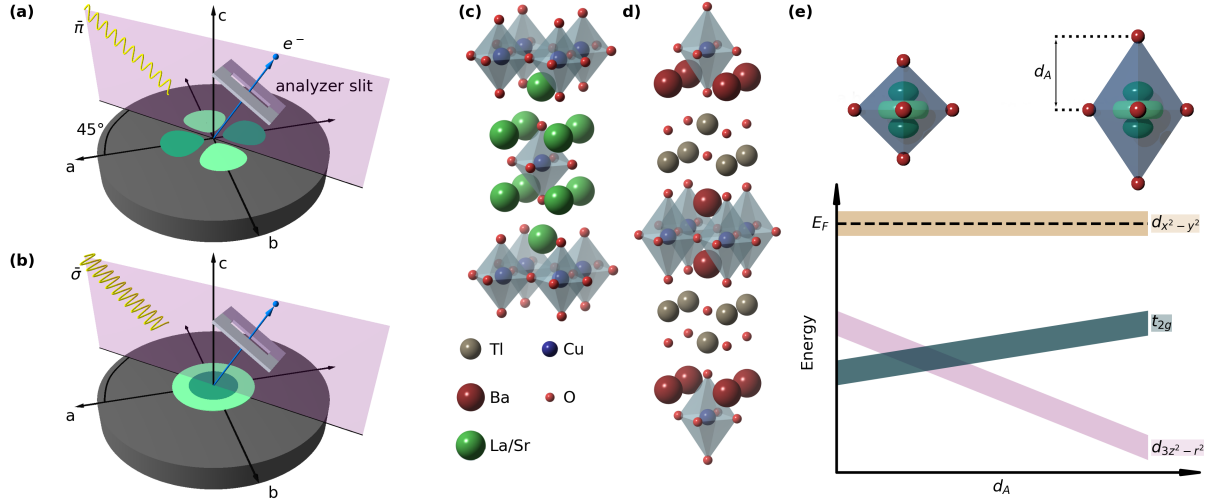


FIG. S4. Photoemission geometry, crystal structures and crystal field splitting. (a),(b) Schematic of the photoemission experimental setup. The projection of the Cu $3d_{x^2-y^2}/d_{3z^2-r^2}$ orbital is visualized at the origin of the coordinate system and a nodal mirror plane defined by the incident photons and photoemitted electrons is indicated. Incoming light polarized perpendicular and parallel with respect to the mirror plane is labeled $\bar{\sigma}$ and $\bar{\pi}$, respectively. (c),(d) Crystal structures of LSCO and Tl2201, respectively. (e) Top: Octahedra of different apical oxygen distance d_A with a representation of the $d_{3z^2-r^2}$ orbital enclosed. Bottom: Schematics of the $d_{x^2-y^2}$, $d_{3z^2-r^2}$ and t_{2g} crystal field splittings as a function of apical oxygen distance d_A .